



## Research papers

# Seasonal recharge mechanism of the upper shallow groundwater in a long-term wastewater leakage and irrigation region of an alluvial aquifer

Shiqin Wang<sup>a,b,c,\*</sup>, Zhixiong Zhang<sup>a,c</sup>, Matthias Sprenger<sup>d</sup>, Shoucai Wei<sup>e</sup>, Wenbo Zheng<sup>a</sup>, Binbin Liu<sup>a</sup>, Yanjun Shen<sup>a,\*</sup>, Yizhang Zhang<sup>f,\*</sup>

<sup>a</sup> Key Laboratory of Agricultural Water Resources, Center for Agricultural Resources Research, Institute of Genetics and Developmental Biology, Chinese Academy of Sciences, Shijiazhuang 050021, China

<sup>b</sup> Xiongan Institute of Innovation, Chinese Academy of Science, Xiongan 071700, China

<sup>c</sup> University of Chinese Academy of Sciences, 19A Yuquan Road, Beijing 100049, China

<sup>d</sup> Lawrence Berkeley National Laboratory, 1 Cyclotron Road, Berkeley CA 94720, USA

<sup>e</sup> Binzhou University, Shandong Provincial Key Laboratory of Eco-Environmental Science for Yellow River Delta, Binzhou 256603, China

<sup>f</sup> Chinese Research Academy of Environmental Sciences, 8 Dayangfang, Anwai Beiyuan, Beijing 100012, China

## ARTICLE INFO

## Keywords:

Recharge processes

Seasonal hysteresis

Stable isotopes

Wastewater leakage

Alluvial aquifer

## ABSTRACT

Understanding the mechanisms that control seasonal groundwater recharge at local and intermediate scales is critical for understanding contaminant transport. The recharge mechanism of seasonal precipitation and irrigation, accompanied by legacy wastewater in porewater in alluvial aquifer were complicated due to the seasonal variation of multiple recharge sources. In this study, a long-term wastewater leakage and irrigation region along the Tanghe Wastewater Reservoir (TWR) in the alluvial plain area of North China Plain to investigate the recharge mechanism from unsaturated zone to the upper shallow groundwater affected by multiple water sources. Water chemical ions and stable isotopes of water ( $^2\text{H}$  and  $^{18}\text{O}$ ) of 30 m deep sediment profiles and groundwater boreholes were used to trace the recharge processes. The porewater stable isotopes of the sediment profiles revealed vertical recharge rates ranging from 0.63 to 1.09 m/year for the layered unsaturated zone with silt and silty clay. Due to the matrix flow through unsaturated zone, the legacy wastewater in the unsaturated zone affected the variation of groundwater quality in long term. However, fast flow (i.e., preferential or lateral flow) occurred in sand layers of alluvial aquifers lead to significant precipitation contributions (44 to 61 %) to the upper shallow groundwater (USGW) recharge, resulting in the seasonal variation of stable isotopes and water chemical ions. Affected by the fast flow with seasonal variations and matrix flow with legacy wastewater in the unsaturated zone, the  $\delta^2\text{H}$  and  $\delta^{18}\text{O}$  relationship of the USGW showed two types of hysteresis loops in the dual isotope space: 1) groundwater in regions affected by the TWR wastewater leakage shows narrow loops and a nearly straight line with end-members of precipitation that recharged to groundwater by fast flow, and evaporated porewater plotting along the TWR evaporation line; and 2) groundwater in irrigated farmlands with low and high irrigation amounts and intense evaporation shows stronger hysteresis with loops overlapping with shallow porewater, suggesting the impact of legacy wastewater of the unsaturated zone on groundwater. The residual pollutants in soil and the type of fast flow determine the different seasonal variation of groundwater quality. Preferential flow in alluvial aquifer regions can increase the proportion of seasonal recharge from precipitation, resulting in the rapid introduction of contaminants from surface or shallow soils into the alluvial aquifer.

## 1. Introduction

Groundwater is the primary water supply in many regions with

rapidly expanding water requirements, including urban, industrial, and agricultural production. Groundwater is particularly important in alluvial aquifers, where groundwater renewal rates are generally high (Ma

\* Corresponding authors at: Key Laboratory of Agricultural Water Resources, Center for Agricultural Resources Research, Institute of Genetics and Developmental Biology, Chinese Academy of Sciences, Shijiazhuang 050021, China (S. Wang).

E-mail addresses: [sqwang@sjziam.ac.cn](mailto:sqwang@sjziam.ac.cn) (S. Wang), [yjshen@sjziam.ac.cn](mailto:yjshen@sjziam.ac.cn) (Y. Shen), [zhangyz@craes.org.cn](mailto:zhangyz@craes.org.cn) (Y. Zhang).

<https://doi.org/10.1016/j.jhydrol.2023.130424>

Received 8 July 2023; Received in revised form 19 October 2023; Accepted 21 October 2023

Available online 6 November 2023

0022-1694/© 2023 Elsevier B.V. All rights reserved.

et al., 2019; Sun et al., 2021), and serves as potable water sources in arid, semi-arid, and semi-humid areas. However, these aquifers are also susceptible to depletion and contamination, with recharge rate and dominant flow processes determining their level of vulnerability (de Vries and Simmers, 2002). Complex hydrological processes controlled by geology, meteorology, morphology, and vegetation influence groundwater recharge. Therefore, identifying recharge sources and mechanisms is essential to develop strategies to prevent groundwater pollution (Jasechko, 2019).

Precipitation or other recharge sources show seasonal characteristics in these areas, which result in seasonal variations of recharge rates, fluxes, and thus the transport of potential contaminants (Tweed et al., 2020). Understanding recharge rates at seasonal timescales can help improve the accuracy of predicting long-term changes in annual recharge rates under changing climate conditions (Niraula et al., 2017; Raihan et al., 2022; Yang et al., 2021). The seasonal timing and relative efficiency of recharge between seasons can be determined using stable isotopes ( $^2\text{H}$  and  $^{18}\text{O}$ ) of groundwater (Sánchez-Murillo and Birkel, 2016; Stahl et al., 2020). However, the seasonal stable isotopic signal of natural recharge disappears in groundwater as the water moves through the thick and low-conductivity vadose zone to the aquifer due to intense mixing (i.e., dispersion) along the flow path (Chen et al., 2017; Wright and Novakowski, 2019). But, when water travels through a thin and coarse size stratum, or preferential flow occurs in the unsaturated zone, the natural recharge maintains the isotopic signals characteristic of seasonal variation, which can also be detected in the groundwater.

Non-natural recharge from leaking infrastructure, stormwater drainage, or dry season irrigation also contributes to groundwater recharge at local and intermediate scales (Grande et al., 2020). While the recharge amount may not be necessary for assessing groundwater quality, it is critical for tracking contaminant transport, as concentrated recharge and preferential flow allow contaminants to migrate rapidly through the unsaturated zone to underlying aquifers. Industrial and domestic effluents are often recharged to aquifers through wastewater treatment plants (McCance et al., 2020), sewage reservoirs, polluted rivers (Beckers et al., 2020), sewage-irrigated farmland (Wu et al., 2015), or broken drainage (Ishii et al., 2021). Long-term wastewater infiltration can cause a degradation of the groundwater quality. Particularly, unlined wastewater reservoirs or ponds can deteriorate regional scale groundwater quality (Gal et al., 2009; Wang et al., 2014).

Stable isotopes of water are effective tracers for describing and quantifying groundwater recharge rates, water flow pathways, response times, and mechanisms under natural and non-natural conditions (Beddows et al., 2016; McGuire et al., 2002; Tekleab et al., 2014; Tipple et al., 2017; Vystavna et al., 2019). The isotopic composition of precipitation varies seasonally, reflecting seasonal shifts in moisture sources, air mass trajectories, and cloud processes (Craig, 1961; Dansgaard, 1964; Rozanski et al., 1993). Stable isotope coupling of precipitation time series with the dynamics of soil water (Garvelmann et al., 2012; Lee et al., 2007; Sprenger et al., 2016) or groundwater (Ma et al., 2017; Wright and Novakowski, 2019) have been used to investigate seasonality and residence time of soil water and groundwater. The processes involved in groundwater recharge, such as mixing and preferential flow, have also been thoroughly researched (Lee et al., 2007; Ma et al., 2017).

Evaporation causes an enrichment of heavy isotopes in water, which differs from meteoric waters (e.g., infiltrating snowmelt or rainfall). The signals from the evaporation distillation of stable isotopes in water can be used to trace the processes of groundwater recharge. Benettin et al. (2018) reported that the reference of the original composition of a water source according to the evaporation line should be valid if the evaporated samples all originate from a single water source. And, for differences between the seasonal cycle of evaporation fractionation and the seasonal cycle of the isotopic composition of water sources, numerical experiments based on established isotope fractionation theory have suggested that residual water samples show a hysteresis loop (Benettin et al., 2018). It has also been suggested that the width of the hysteresis

loops depends on the amplitude of the seasonal cycle of evaporation and the extent to which it differs from the seasonal cycle of precipitation isotopes. However, not only are there seasonal differences in water sources and evaporation in field studies, but for groundwater in agricultural areas, it is still unclear how multiple water sources, such as precipitation, irrigation, wastewater leakage, and water held in unsaturated zones, affect the hysteresis loops.

Previous research has identified seasonal recharge (Ma et al., 2017) and seasonal contamination (Vystavna et al., 2019) in alluvial aquifers in temperate climates using a combination of stable isotopes and hydrochemical methods. In some alluvial aquifers, pumping of irrigation water from groundwater sources leads to a decrease in groundwater levels, and irrigation return flows may then experience strong seasonal evaporation effects, altering the hydrological cycle. Intensive irrigation and wastewater leakage accelerate infiltration and recharge of water and transport of solutes to groundwater (Gal et al., 2009). Under the impact of multiple water sources (precipitation, wastewater leakage, and irrigation), little is known about the seasonal effects of these multiple water sources on the evaporation of soil water and groundwater and therefore on groundwater recharge.

In this study, a linear wastewater reservoir in the Xiong'an New Area, in the Baiyangdian Lake watershed of the North China Plain (NCP), was selected as a case study. The reservoir is unlined and was built along a river channel for storing industrial wastewater from 1977 to 2015. Over-pumping groundwater for irrigation has led to groundwater decline in the alluvial aquifer of the NCP (Wang et al., 2008). Therefore, the wastewater was stored in the reservoir and lost as evaporation, leakage, and agricultural irrigation. The impact of the wastewater reservoir on shallow groundwater has been studied by using an evaporation and recharge model based on isotope fractionation theory (Wang et al., 2014). However, the recharge process with varying and multiple recharge sources was still unclear. Due to evaporation, the isotopes in the wastewater have a strongly enriched signal which can be used to trace which processes are occurring during groundwater recharge.

This research applied a multi-tracer method to investigate the seasonal mechanisms of groundwater recharge as affected by long-term wastewater leakage under a complex system of natural and non-natural recharge sources (sewage irrigation and groundwater irrigation). This paper aims to understand the mechanisms and hysteresis loops that control seasonal groundwater recharge in alluvial aquifers affected by multiple recharge sources.

## 2. Materials and methods

### 2.1. Study site

Our study site was located in the middle of the Tanghe Wastewater Reservoir (TWR) in the Xiong'an New Area of the Baiyangdian Lake watershed, 9.5 km west of Baiyangdian Lake (BL) (Fig. 1a). A continental monsoon climate with a strong seasonality characterizes the site. Based on 42-year climate data from 1977 to 2019 (Fig. 1b), the mean annual temperature is 13.3 °C, and the mean annual precipitation is 504 mm. Summer months (June–August) are relatively hot and humid, with an average monthly temperature of 26.3 °C and precipitation of 115 mm. The winters (December - February) are cold and dry, with an average monthly temperature of -1.0 °C and precipitation of 3 mm. The potential evapotranspiration is 1208 mm/year, and the evaporation from March to June is higher than during other months.

The reservoir is unlined and was built along the northern part of the Tanghe River Channel (Fig. 1c) for storing untreated industrial wastewater with high sulphate concentrations from Baoding City for almost 38 years (from 1977 to 2015). It was connected to the BL by a sluice gate in the east, which severely affected the water quality of the BL. The TWR has a total length of 17.5 km, a water surface width of about 100 m, and a storage capacity of  $7.2 \times 10^6 \text{ m}^3$ . The northern embankment of the

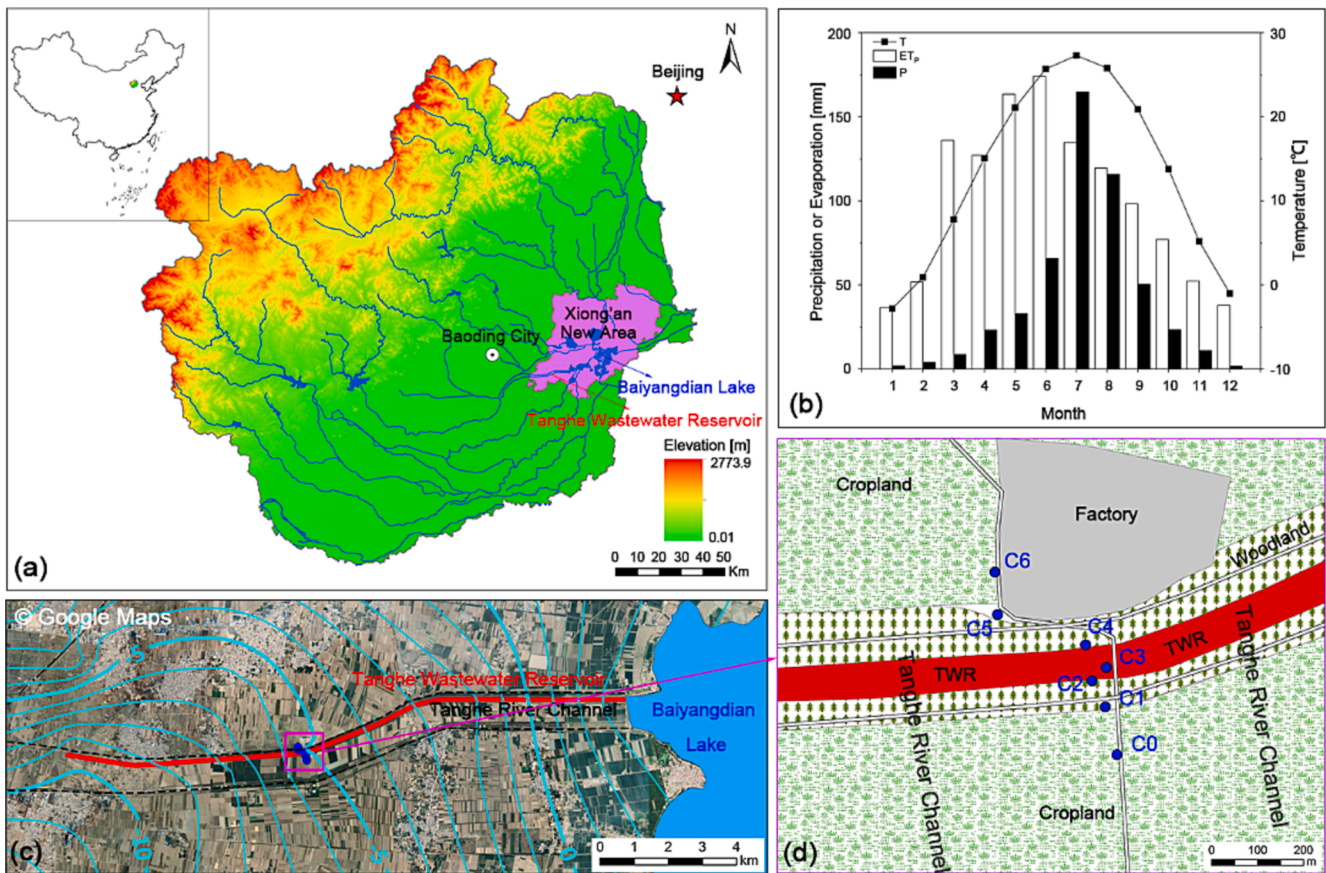


Fig. 1. Geographical location of the Tanghe Wastewater Reservoir (TWR) and soil sampling sites. (a) Position of the TWR in the Baiyangdian Lake watershed. (b) The mean monthly precipitation (P) and potential evapotranspiration (ET<sub>p</sub>) over the study period (1977–2019). (c) Position of the study transect in the middle of the TWR and the flow map of the unconfined aquifer around TWR in November 2018. (d) Sampling sites along the transect.

TWR was the original Tanghe River embankment, constructed in 1966, while the southern embankment was compacted from the silty sediment excavated from the TWR channel, both embankments being about 180 m apart. The Tanghe River has been drying up for several decades due to the interception of the reservoir upstream in the mountains, and the over-pumping of groundwater in the plain, and a large amount of wheat/maize is planted in the channel. After the TWR started to store wastewater in 1977, the impacts of anthropogenic activities on the TWR varied greatly (Fig. 2). The amount of wastewater entering the reservoir was reduced and stopped in the middle part of the channel in 2010. The effluent inflow was intercepted entirely in 2015. Due to the development

of the Xiong'an New Area in 2017, the wastewater that remained in the reservoir was removed in 2018.

TWR is located in the floodplain with flat terrain, and the surface elevation of the profile at the study site is 6–10 m. According to the regional hydrogeological survey, the 30 m depth range consists of Quaternary Holocene and Late Pleistocene alluvial sediments with a high level of permeability and heterogeneity, in which the unsaturated zone is interlayered with silt and silty clay, and the saturated zone comprises silt and sand with local inclusions of thick layers of silty clay. The Tertiary-Quaternary aquifers are usually divided into shallow and deep groundwater at the study site. Still, our present study is concerned

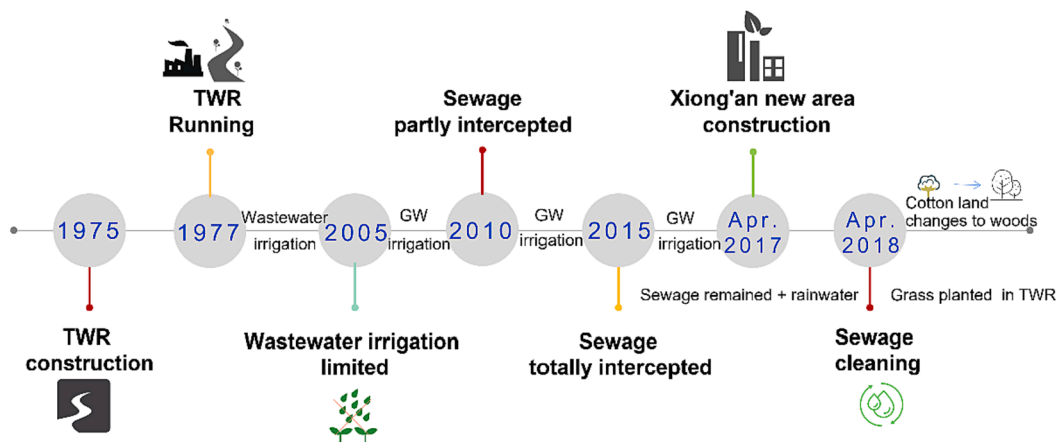


Fig. 2. Impact of anthropogenic activities on the TWR over the past four decades.

with groundwater below 30 m, which we refer to as the upper shallow groundwater (Fig.S1). During the wastewater storage period of TWR, the upper shallow groundwater flows from north to south, and the groundwater level inside the reservoir is higher than that outside the embankments (Wang et al., 2013). On a regional scale, the over-pumping of groundwater has led to the drying up of natural rivers and lakes and the lowering of groundwater levels. However, artificial water recharge to the BL has raised the water table around the lake, and the groundwater levels around TWR are higher in the east and lower in the west (Yuan et al., 2020; Yuan et al., 2017). Groundwater flows from the northeast to the southwest with a hydraulic gradient of 0.5‰–1.3‰ in the middle of TWR in Fig. 1c (by kriging interpolation with the groundwater level data measured in November 2018). The average groundwater depth along the profile is 12.7 m and the permeability of the upper shallow aquifer is 4.66 m/d. The primary land use around the TWR is wheat/maize, which refers to the rotation of wheat sown in winter and maize sown in summer (Fig. 1c and d). The wastewater from the TWR was mainly used for agricultural irrigation during the past several decades. In recent years, shallow groundwater (80–120 m depth) has been used for irrigation. In addition to the irrigation return flow of wastewater and shallow groundwater, wastewater infiltration is another primary groundwater source along the TWR. It was estimated that 76% of the wastewater recharges to the groundwater through leakage and irrigation, and the area of influence was approximately 3 km around the TWR and down to 150 m depth of the aquifer (Wang et al., 2014).

Our study area was located in the middle of the TWR, which has a large industrial factory near the observation profiles north side (Fig. 1d). Additionally, there were many small factories in the north of the TWR according to the field investigation. Crops are cotton and wheat/maize in the north and south, respectively. In April 2018, cotton was converted into woods, and grass was planted in the TWR channel (Fig.S2). To distinguish from the shallow groundwater in the region, the upper shallow groundwater (USGW) is used in this paper to represent the groundwater at 30 m depth. Also, the references to shallow groundwater (SGW, 80–120 m) and deep groundwater (DGW, 120–300 m) refer to groundwater samples collected at 80–120 m and 120–300 m, respectively, for identifying the proportion of groundwater irrigation.

## 2.2. Fieldwork and sampling

This study focused on a 480 m long transect perpendicular to the TWR, where we sampled the sediment and groundwater. Seven 30 m deep sediment profiles were drilled along the transect with an air flush rotary drill during 8th to 19th June 2017. From south to north, the profiles are referred to as C0, C1, C2, C3, C4, C5, and C6 (Fig. 1c). The C3 profile was located in the middle of the TWR channel, which was essentially dry at the time of sampling, with only a small amount of effluent present in a low-lying area to the west of C3. C1 and C5 were located outside the north and south embankments of the TWR, respectively, immediately adjacent to the embankments. Profiles C0 and C6 were about 150 m from the reservoir embankments and located in agricultural fields growing wheat/maize and cotton, respectively.

Sediment samples from five profiles (excluding C2 and C4) were collected at 0.1, 0.2, 0.3, 0.5, 0.7, and 1.0 m, at 0.5 m intervals from 1 to 10 m depth, and at 1.0 m intervals from 10 m to 30 m depth, with additional sediment samples taken at depths where the texture changed. Sediment samples collected using aluminum boxes were primarily used to determine the gravimetric moisture content. Sub-samples of the sediment samples were collected and sealed in small brown glass vials and stored in a  $-20^{\circ}\text{C}$  refrigerator until the stable isotopic compositions of the porewater were analyzed. Sub-samples of the sediment samples were packed into Ziploc bags to analyze major water chemical ions. In addition, the vertical and horizontal undisturbed 0.1 m sediment cores were collected with ring samplers and used to determine the porosity and saturated hydraulic conductivity.

After collecting the sediment samples, 30-meter polyvinyl chloride

(PVC) pipes were installed in the borehole to construct groundwater monitoring wells. The screen depths were at 15–25 m depth. Groundwater samples from the monitoring wells (C0, C1, C3, C5, and C6) were collected monthly from October 2017 to June 2019. In addition, wastewater was sampled at the study site in June 2017, and both shallow groundwater (80–120 m) and deep groundwater (120–300 m) were sampled over a 2.5 km area along the Tang River.

All water samples were collected in PVC bottles (50 mL) and taken to the laboratory for storage at  $4^{\circ}\text{C}$ . The groundwater level was determined at each sampling using a water level measuring ruler. The pH, electrical conductivity (EC), oxidation–reduction potential (ORP), and temperature were measured in situ using a portable meter (WM-22EP, DKK, TOA Corporation of Japan).

## 2.3. Chemical and isotope analysis

We derived the gravimetric sediment moisture content via oven drying ( $105^{\circ}\text{C}$ , 12 h) and converted this to sediment moisture content based on the measured bulk weight. Sediment bulk density was estimated by relating the oven-dried sediment weight to the sediment sample core volume.

Sediment samples for analysis of major ions ( $\text{Na}^+$ ,  $\text{K}^+$ ,  $\text{Ca}^{2+}$ ,  $\text{Mg}^{2+}$ ,  $\text{Cl}^-$ ,  $\text{SO}_4^{2-}$ , and  $\text{NO}_3^-$ ) were dried and ground, and chemicals in solution were determined by extraction of soluble salts using a mass ratio of sediment to ultrapure water of 1: 5. The extracted water, wastewater, and groundwater were filtered through  $0.45\ \mu\text{m}$  and  $0.2\ \mu\text{m}$  filters, respectively. The major ions were then measured by ion chromatography (ICS-2100, Dionex, U.S.A.).

Sediment porewater was extracted by the automatic water extraction system (LI-2100, LICA, China) for 3 h, separated by evaporation at  $125^{\circ}\text{C}$ , and collected by condensation at  $-94^{\circ}\text{C}$  with a system pressure of 1000 pa. We analyzed the extracted porewater, wastewater, and groundwater for their oxygen and hydrogen isotopes at the Key Laboratory of Agricultural Water Resources, Chinese Academy of Science via a laser absorption water–vapor isotope analyzer (Picarro-i2120, CA, U.S.A.). The stable isotope ratios are expressed in delta ( $\delta$ ) units and a per mil (‰) notation relative to the Vienna Standard Mean Ocean Water (VSMOW). The reported analytical errors for oxygen and hydrogen isotope ratios are  $\pm 0.1\ \text{‰}$  for  $\delta^{18}\text{O}$  and  $\pm 1\ \text{‰}$  for  $\delta^2\text{H}$ , respectively.

## 2.4. Data analysis

### 2.4.1. Spectrum analyses and groundwater response time

The spectrum of a signal is a typical way of investigating the frequency distribution of a time series. Fundamental work on spectral analysis of groundwater systems was carried out by Gelhar and Wilson (1974). Recently, this method has often been used to study groundwater recharge, recharge timescales, and spatial scale variability (He and Guan, 2020; Houben et al., 2022). Spectral analysis of stable signals often uses the sine wave method to convert the signal into a regular trigonometric form (Beddows et al., 2016; Das et al., 2021). We estimated the response time based on the sine wave approach fitting the seasonal signal of water isotopes in rainwater and groundwater (Beddows et al., 2016).

$$\delta = \delta_0 + \delta_A \sin\left(\frac{(t - t_0)2\pi}{\tau}\right) \quad (1)$$

$$\Delta t = t_{02} - t_{01} + n\tau \quad (2)$$

where  $\delta$  is either  $\delta^2\text{H}$  or  $\delta^{18}\text{O}$ ,  $\delta_0$  is the sine offset on the  $\delta$  axis,  $\delta_A$  is the amplitude of the sine function,  $t$  = date,  $t_0$  = date where the sine phase equals zero, and  $\tau$  is the period of the sine function,  $t_{01}$  and  $t_{02}$  are the dates where the sine phase equals zero for precipitation and groundwater, respectively,  $n$  is the number of periods of the actual response time of the precipitation and groundwater signals.

2.4.2. Exponential model and groundwater residence time

The seasonal variability of stable isotopes in the precipitation is often reflected in the isotopic variability of river- and groundwater (Grande et al., 2020; Zhou et al., 2021). The composition of outflows at any time,  $\delta_{out}(t)$ , is made up of past inputs lagged,  $\delta_{in}(t-\lambda)$ , according to their residence time distribution,  $g(\lambda)$ .

$$\delta_{out} = \int_0^{\infty} g(\lambda)\delta_{in}(t-\lambda)d\lambda \quad (3)$$

where  $\lambda$  is the lag times between input and output tracer composition.

In previous studies, the transfer function  $g(\lambda)$  was often generalized as an exponential model (Rodgers et al., 2005; Zhou et al., 2021).

$$g(\lambda) = \frac{\exp(-\frac{\lambda}{T})}{T} \quad (4)$$

where  $T$  is the residence time.

Based on spectral analysis and the exponential model, the mean groundwater residence time can be expressed as (McGuire et al., 2002; Tekleab et al., 2014):

$$T = \frac{\tau}{2\pi} \sqrt{\left(\frac{\delta_{A1}}{\delta_{A2}}\right)^2 - 1} \quad (5)$$

where,  $\delta_{A1}$  and  $\delta_{A2}$  are the amplitudes of the sine function for precipitation and groundwater, respectively.

3. Results

3.1. Subsurface characterization

Geologic borings revealed multiple layers of silt, silty clay, and sand of varying thicknesses (Fig. 3). The elevation of the transect ranged from 6 to 10 m above sea level. There were two sand layers within 30 m depth. The depth of the first sand layer ranged from 8 to 12 m and was thickest beneath the TWR (Fig. 3). The depth of the second sand layer ranged from 22 to 28 m, with a thickness of about 2 m. Silty clay layers under the TWR channel constituted a weakly permeable aquifer that connected the wastewater to the TWR. A field survey found that black/brown sediments extended along this silt layer from north and south, suggesting a possible lateral pathway of wastewater transport due to the

Fe or Mn contained wastewater. In the unsaturated zone, the porosity of silt and silty clay layers are 0.41 and 0.40, and the vertical saturated hydraulic conductivity of the silt and silty clay layers are  $1.5 \times 10^{-2}$  and  $6.8 \times 10^{-3}$  m/d. The thickness of the silty clay layer in the north is less than that in the south, indicating that the permeability of the vadose zone in the northern farmland is higher than that in the south. In the saturated zone, the horizontal permeability coefficients of the sand, silt, and silty clay layers were 4.66,  $1.1 \times 10^{-2}$ , and  $8.9 \times 10^{-3}$  m/d, respectively. The northern farmland location is mainly sand and silt layer. In contrast, the southern farmland is primarily sand and thick silty clay layers, and the thickness of the upper sand layer is small, indicating that the hydraulic conductivity of the aquifer (<30 m) on the north side is higher.

3.2. Stable isotopes and major ions in wastewater

The stable isotopes of water and major ions of wastewater in the TWR at different times are presented in Fig. 4. The stable isotopes of wastewater in the TWR showed  $\delta^2H$  and  $\delta^{18}O$  compositions of  $-50.9$  and

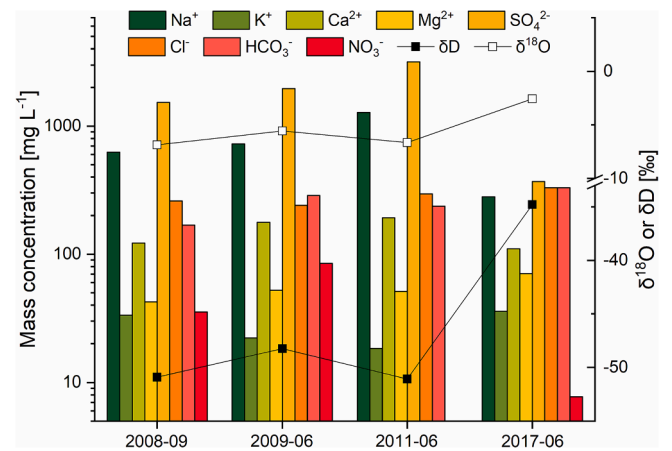


Fig. 4. Variation of stable water isotopes and major ions in wastewater of the TWR. All data are from our actual historical monitoring, among which data for 2008 and 2009 have been published in previous works (Wang et al., 2014).

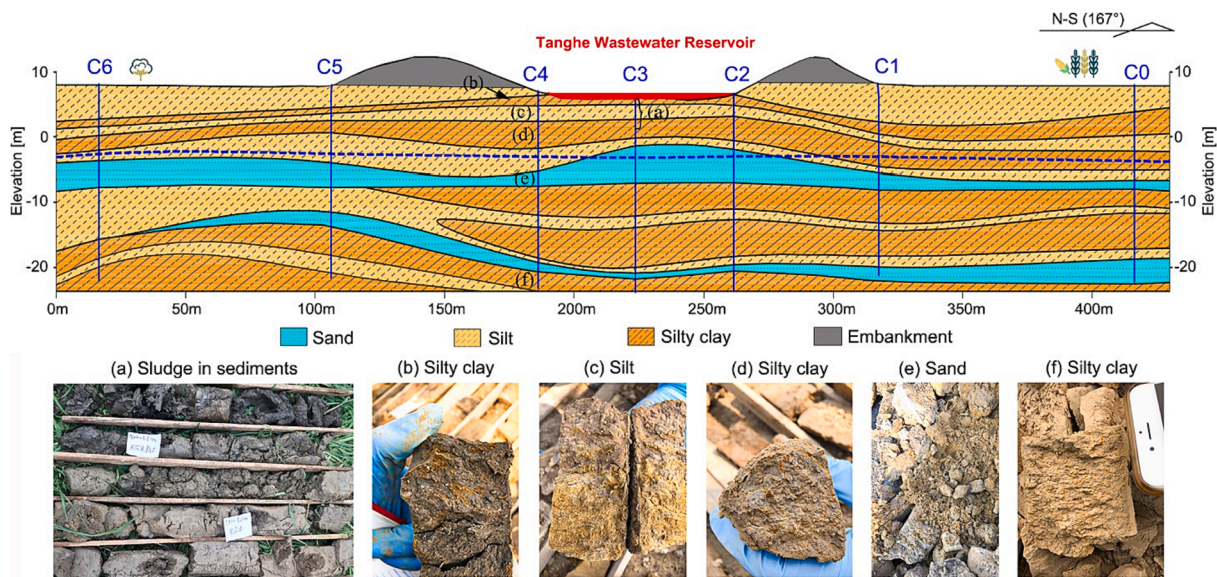


Fig. 3. Profile along the section in the middle part of the TWR. The dashed blue line is the groundwater level. The blue vertical stripes represent the location and depths of the profiles, and the photos (a) to (f) represent extracts from the boreholes with their locations identified with the letters in the vertical profile. Sediment profiles C0-C6 are projected in the direction perpendicular to TWR.

−6.9 ‰ in September 2008, respectively, and −48.3 and −5.6 ‰ in June 2009. As there was no wastewater inflow after 2015, the wastewater progressively evaporated, whereby the  $\delta^2\text{H}$  and  $\delta^{18}\text{O}$  compositions enriched to −34.8 and −2.6 ‰, respectively, by June 2017. The high concentrations of  $\text{Na}^+$  and  $\text{SO}_4^{2-}$  were indicative of wastewater in the TWR. The  $\text{Na}^+$  and  $\text{SO}_4^{2-}$  concentrations increased from September 2008 to June 2011 (i.e.,  $\text{SO}_4^{2-}$  concentrations increased from 1528.3 to 3171.0 mg/L). After the TWR interception in 2015, the concentration of  $\text{Na}^+$  and  $\text{SO}_4^{2-}$  decreased to 280.9 and 369.1 mg/L, respectively, in June 2017 (Fig. 4).

All wastewater isotopes plotted closely around the TWR evaporation line ( $\delta^2\text{H} = 4.93 \times \delta^{18}\text{O} - 20.99$ ,  $R^2 = 0.99$ ), estimated from the isotopes of wastewater collected by previous work (Wang et al., 2014). Wang et al. (2014) reported that the wastewater stored in the TWR was enriched in heavy stable isotopes due to evaporation. As  $\text{Na}^+$  is easily absorbed in clay or silt clay, the indicative ions of  $\text{SO}_4^{2-}$  companies with the enriched isotopes of wastewater will be applied as tracers to investigate the impact of the wastewater on porewater and groundwater.

### 3.3. Stable isotopes in porewater

The variations of  $\delta^2\text{H}$  and  $\delta^{18}\text{O}$  in porewater throughout the sediment profiles of C0, C1, C3, C5, and C6 are presented in Fig. 5. The stable isotopes of different sites show gradual enrichment (C0, C1, C6) or depletion (C3) trends with depths due to the infiltration of different water sources. To identify the stable isotopes characteristics, the depth profiles were divided into three groups (Fig. 5): (I) The top silt layer (above the first silty clay layer, where there was little evidence of the wastewater leakage); (II) From the top of first silty clay layer to the top of first sand layer, where wastewater might penetrate the silt and silty clay reaching the first aquifer; and (III) Depth from the top of the first sand layer to the bottom of the second sand layer. The stable isotopes in the upper of Group II in the C3 profile (0–3.0 m, excluding 0.6 m) were most enriched and were less variable, with  $\delta^2\text{H}$  ranging from −49.1 to −47.2 ‰ and  $\delta^{18}\text{O}$  ranging from −5.2 to −4.1 ‰. Then the stable isotopes showed a depleting trend from 3.0 to 6.5 m with peak values of −61.9 and −7.4 ‰ for  $\delta^2\text{H}$  and  $\delta^{18}\text{O}$ , respectively (Fig. 5). These

variations are consistent with the variations in the progressively enriched isotopes in the wastewater of TWR from 2011 to 2017 (Fig. 4), the average recharge rate of wastewater was estimated to be 1.09 m/year. Differing from the C3 profiles, the stable isotopes in C0 and C6 increased from the surface (Group I) with increasing depths (Group III), except for the silty clay depths deeper than 22.5 m. This was consistent with the increasing variation in isotopes from irrigation water with SGW at present (mean  $\delta^2\text{H}$ : −62.5 ‰; mean  $\delta^{18}\text{O}$ : −7.9 ‰) and with wastewater (mean  $\delta^2\text{H}$ : −46.0 ‰; mean  $\delta^{18}\text{O}$ : −5.4 ‰) historically, we estimated recharge rates of 0.63 and 0.75 m/year for C0 and C6, respectively. The ranges in isotopes in C6 (from −88.3 to −43.9 ‰ and from −10.6 to −2.25 ‰ for  $\delta^2\text{H}$  and  $\delta^{18}\text{O}$ , respectively) were more extensive than in C0 (from −70.4 to −45.7 ‰ and from −8.8 to −2.9 ‰ for  $\delta^2\text{H}$  and  $\delta^{18}\text{O}$ , respectively).

The mean isotopic values in Group I and III in C6 were greater than in C0. This discrepancy can be attributed to the different infiltration mechanisms for irrigation water in the cotton and wheat/maize, the evaporation in the cotton land with less irrigation (100 mm/a (Min et al., 2018)) caused the isotopes in sediment water to get more enriched than those in the wheat/maize cropping system with more irrigation (320–360 mm/a (Sun et al., 2006; Zhang et al., 2018)). The C1 and C5 profiles were located outside of the TWR embankment. The stable isotope distributions in C1 and C5 had greater enrichment with greater depth, also observed in the isotopes in the silty clay layers at deep depths. This is consistent with the impact of precipitation, which has a more depleted isotopic signature than wastewater.

There were similarities in sediment profile porewater  $\delta^2\text{H}$  and  $\delta^{18}\text{O}$  trends in C1, C3 and C5, and in C0 and C6 (Fig. 6). All profiles showed isotopic values that plotted in the dual isotope space beneath the evaporation line of the TWR (Fig. 6). The slope of the fitting line for the porewater isotopes of C3 and C1 were similar to that of TWR, with slopes of 4.87 and 4.65, respectively (C3:  $\delta^2\text{H} = 4.65 \times \delta^{18}\text{O} - 25.68$ ,  $R^2 = 0.95$ ; C1:  $\delta^2\text{H} = 4.87 \times \delta^{18}\text{O} - 25.54$ ,  $R^2 = 0.95$ ), suggesting the impact of partly evaporated wastewater on porewater. There were few samples in the sand layers where C1 showed extreme deviation from the TWR evaporation line (labeled in Fig. 6a). The samples taken from C5 were clustering in a similar location in the dual isotope space as Group III of

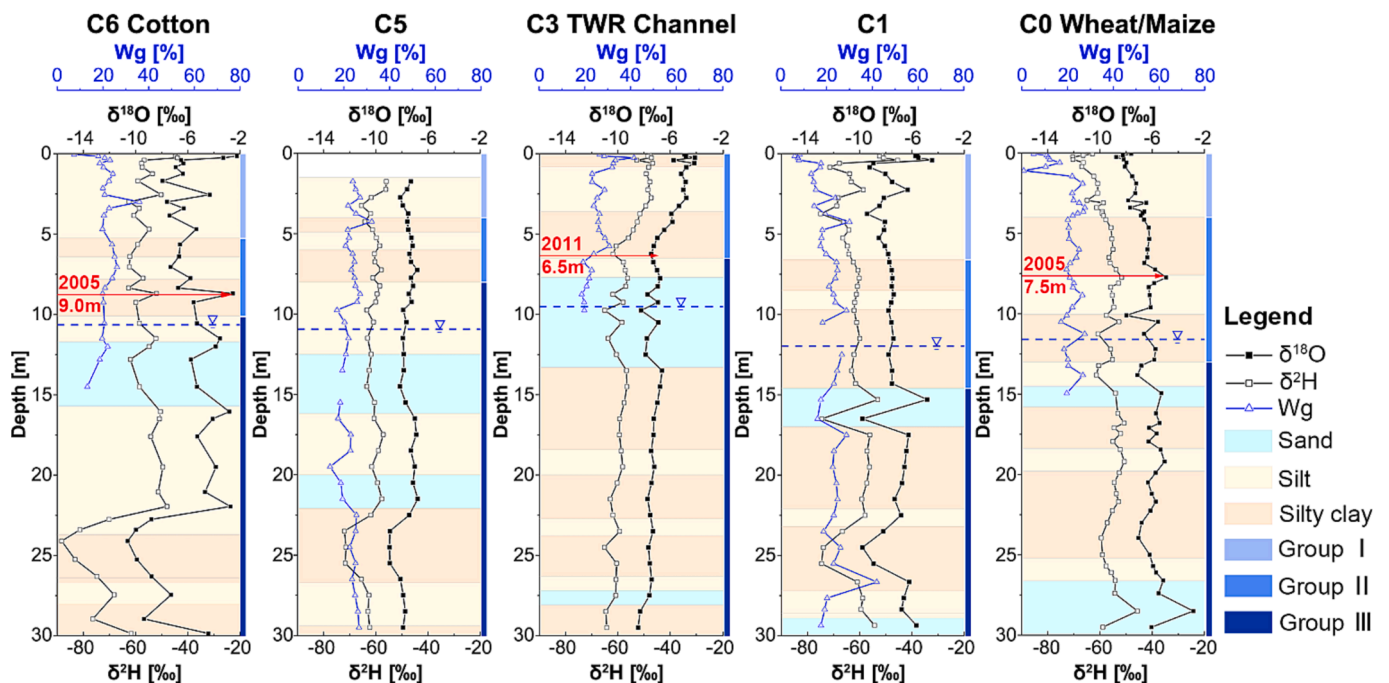
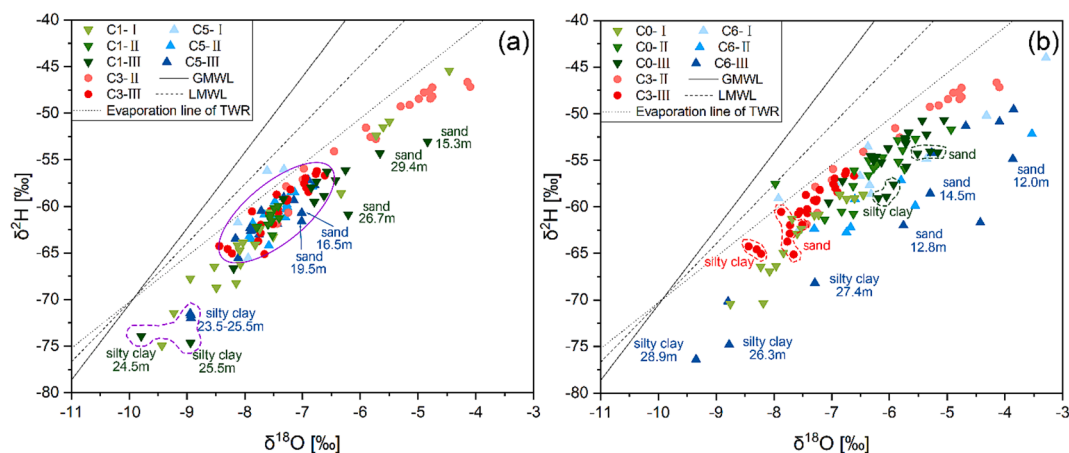


Fig. 5. Vertical distribution of stable isotopes and gravimetric water content (Wg) in porewater for profiles C0–C6. The horizontal red lines represent depths indicating a vertical variation in sources.



**Fig. 6.** Relationship between  $\delta^2\text{H}$  and  $\delta^{18}\text{O}$  in porewater throughout the sediment profiles. (a) Sediment profiles C1 and C5 compared with C3; (b) Sediment profiles C0 and C6 compared with C3. The number I, II, and III in legends were groups of different layers as defined in Fig. 3. The global meteoric water line (GMWL) is from (Craig, 1961). The local meteoric water line (LMWL) was obtained from the precipitation data for Shijiazhuang City near the study area. The TWR evaporation line is  $\delta^2\text{H} = 4.93 \times \delta^{18}\text{O} - 20.99$ ,  $R^2 = 0.99$  (Wang et al., 2014).

C3, and Groups II and III of C1 (solid purple line in Fig. 6a). This excluded several samples from the deep silt clay layers (purple dashed line in Fig. 6a). Samples from C0 and C6 were not distributed close to the TWR evaporation line (Fig. 6b). Samples from C6 showed greater deviation from the evaporation line than C0 ( $C6: \delta 2\text{H} = 2.60 \times \delta 18\text{O} - 41.72$ ,  $R^2 = 0.79$ ;  $C0: \delta 2\text{H} = 4.13 \times \delta 18\text{O} - 30.90$ ,  $R^2 = 0.83$ ). All of these samples deviated far from the LMWL and the TWR evaporation line, suggesting the influence of strong evaporation before and during the infiltration of wastewater irrigation on farmlands. We further found that the porewater samples from the sand aquifers at each site were most

isotopically enriched, and samples from deep silt clay layers were most depleted in heavy isotopes.

### 3.4. Stable isotopes in USGW

The stable isotopes in precipitation and the upper shallow groundwater showed seasonal variation from October 2017 to July 2019 (Fig. 7). The isotopes in the rainfall in the North China Plain were isotopically depleted in the summer and the winter due to the differing effects of air moisture sources (Yamanaka et al., 2004). The input signal

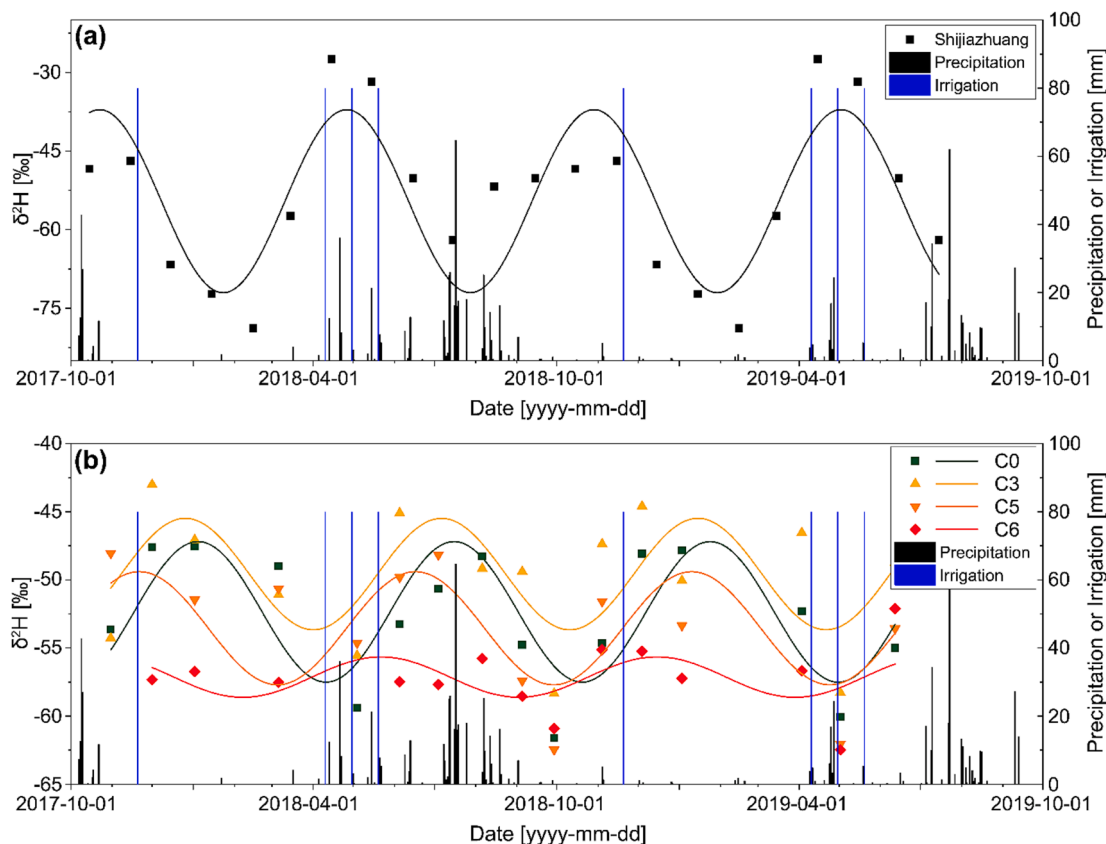


**Fig. 7.** Variations of  $\delta^2\text{H}$  in rainwater (a) and the upper groundwater (b) from November 2017 to June 2019. C1 was not shown in this figure due to the bad fitting coefficient.

of isotopes displays the two peaks with high isotope values during the irrigation season (spring and autumn) (Fig. 7a). SGW (at 80–120 m depth) used for irrigation also had a relatively depleted isotopic signature (mean  $\delta^2\text{H}$ :  $-62.5\text{‰}$ ; mean  $\delta^{18}\text{O}$ :  $-7.9\text{‰}$ ). Corresponding to this, the peaks of depleted isotopes in USGW occurred in April during spring irrigation and in October after the rainy season (Fig. 7b). The seasonal variation of recharge sources had an impact on USGW.

When comparing the USGW of the five sites, USGW at C3 was more enriched in heavy isotopes than at the other sites, with C3 having mean values of  $-49.2$  and  $-5.4\text{‰}$  for  $\delta^2\text{H}$  and  $\delta^{18}\text{O}$ , respectively. This indicated a more significant impact of isotopically enriched wastewater on USGW under the TWR channel. The ranges of stable isotopes in C0, C1, and C3 sites were more extensive than in C5 and C6, suggesting the USGW at the south sites were more easily affected by changing surface condition than the north sites.

Each site's response time and residence time of USGW was calculated using Eqs. (1)–(5) and presented in Table 1. There was a large discrepancy between the results calculated from  $\delta^2\text{H}$  or  $\delta^{18}\text{O}$ . Since  $\delta^{18}\text{O}$  is more affected by evaporation fractionation (Filippini et al., 2015), the  $\delta^2\text{H}$  results were used to investigate the residence and response times to precipitation or irrigation signals. The residence time for USGW from C6 to C0 decreased from 382 to 97 days. Similarly, the response time for USGW from C6 to C0 increased from 266 to 118 days. C6 had a longer groundwater response time than C0, which seems to contradict each other with the description of the permeability of the hydrogeologic unit in part 3.1. In fact, the latter is the description of the thickness and distribution of the weakly permeable layer (silty clay layer), which represents the permeability of the unsaturated zone as a whole, and is consistent with the permeability rate of matrix flow calculated in part 3.3 ( $C6 > C0$ ). And the phenomenon that the response of C0 groundwater level to precipitation is preferred over C6 (Fig. S3) can verify the accuracy of groundwater response time, which can further prove that the development rate of preferential flow is higher in wheat and maize farmland (C0) than cotton farmland (C6) on the outside of the embankment in the river channel zone. The discussion on the effect of preferential flow on groundwater recharge will be continued in Section 4.2.

### 3.5. Sulphate and nitrate in USGW

Fig. 8 shows the monitoring results for indicative ions of  $\text{SO}_4^{2-}$  and  $\text{NO}_3^-$  concentrations in USGW affected by wastewater. The  $\text{SO}_4^{2-}$  concentrations tended to decrease over the monitoring period (Fig. 8a). Mean  $\text{SO}_4^{2-}$  concentrations decreased over time with maximum and minimum values of 1420.9 mg/L and 496.1 mg/L, respectively. Sulphate concentrations were slightly higher during the dry season than in the wet season. Spatially, the  $\text{SO}_4^{2-}$  concentrations at C3 and C5 sites were higher than at farmland sites C0 and C6 before June 2018, when wastewater in the TWR was cleaned. The variation in concentrations for these sites reversed after that time. However,  $\text{NO}_3^-$  concentrations differed significantly, showing a sudden increase and decrease in response to precipitation and irrigation, with a maximum value of 40.8 mg/L (Fig. 8b). The high concentration peaks were observed in June or July after intense rainfall and in May or June after spring irrigation of farmland, and there is also a slight increase in  $\text{NO}_3^-$  from January to March. The mean  $\text{NO}_3^-$  concentrations in USGW at different sites were related to the land surface conditions, with the highest value at the TWR channel (C3), the second highest value in wheat/maize crop at C0, and the third highest value in corn crops (C6), and the lowest value at the two sides of the TWR embankment (C1 and C5).

## 4. Discussions

### 4.1. Infiltration processes affected by multiple recharge sources

As Fig. 5 and Fig. 6 show, the stable isotopes in the five sediment

**Table 1** Mean response times ( $\Delta t$ ), residence times (T), and corresponding fitting parameters of precipitation and groundwater using the trigonometric function. Note: C1 was not shown in this table due to the large fitting error.

Sites	$^2\text{H}$		$^{18}\text{O}$		$^2\text{H}$		$^{18}\text{O}$		$^2\text{H}$		$^{18}\text{O}$		$^2\text{H}$		$^{18}\text{O}$	
	$R^2$	$\delta_0$ (‰)	SE	$\delta_0$ (‰)	$\Delta t$ (d)	SE	$\Delta t$ (d)	SE	$\Delta t$ (d)	SE	$\Delta t$ (d)	SE	T (d)	SE	T (d)	SE
C0	0.56	-52.35	0.9	-6.47	118	0.43	143	11	97	2	34	1				
C3	0.34	-49.58	1.2	-5.54	100	0.58	108	17	125	3	28	1				
C5	0.47	-53.55	1.29	-6.97	85	0.53	72	103	133	4	149	7				
C6	0.19	-57.14	0.81	-6.35	266	0.27	102	17	382	13	91	4				
GNIP	0.70	-52.64	2.85	-7.69	17.19	0.72	2.41	3.96	-	-	-	-	-	-	-	-

Shijiazhuang

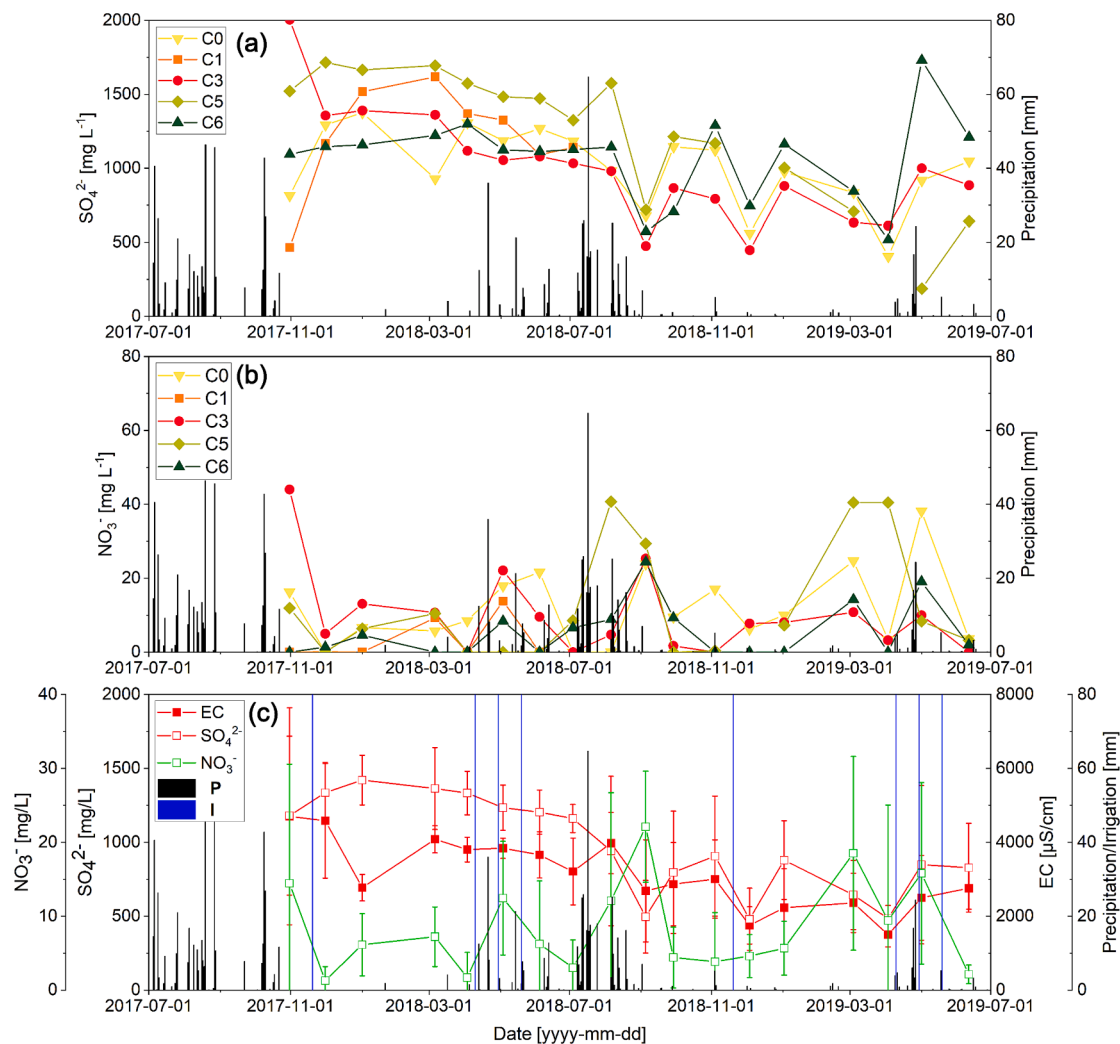


**Fig. 8.** Variations of major ions in the upper shallow groundwater in boreholes along the section from November 2017 to June 2019. (a)  $\text{SO}_4^{2-}$ ; (b)  $\text{NO}_3^-$ ; (c) mean values for EC,  $\text{SO}_4^{2-}$  and  $\text{NO}_3^-$  of all boreholes (the error bars indicate the ranges).

profiles indicated differences in infiltration processes and water sources in porewater when wastewater remained in the TWR channel. All profiles had an obvious isotopic peak point showing the vertical variation in sources. These points were located at 9, 4.5, 6.5, 8.8, and 7.5 m for C6, C5, C3, C1, and C0, respectively (Fig. 5), suggesting infiltration and mixing of different sources. For example, the C3 profile contained wastewater from the TWR and the enrichment of  $\delta^2\text{H}$  and  $\delta^{18}\text{O}$  from deep to shallow depths indicates infiltration and mixing of the more enriched wastewater in the TWR after 2011 with previously recharged wastewater (Fig. 3). The enrichment of stable isotopes in deep layers (>6.5 m depth) and the quickly enriched isotopes in shallow layer (<6.5 m depth) of the C3 profile were in accordance with the stable isotopes in the wastewater of the TWR before 2011 and the greater enrichment from 2011 to 2017, respectively. These recharge rates range from 0.41 to 2.00 m/year, as evaluated by previous research in the alluvial plain of the North China Plain (Min et al., 2018; Wang et al., 2019). Due to the high sediment moisture under wastewater (Fig. 5), the recharge rate of C3 was higher than the cropped fields of C0 and C6. The relatively greater recharge rate in the cotton field of C6 compared to the wheat/maize field of C0 can be attributed to the somewhat thinner silt layer in C6.

Profiles C1 and C5 were located outside of the TWR embankment. A T-test showed that isotopes in the C1 and C5 profiles were similar to that of C3. This indicated that the local lateral flow of TWR wastewater through the vadose zone affects the stable isotopes of porewater in C5

and C1. This was verified by a field survey that found the polluted sludge distributed along the silt clay layer under 4.5 and 8.8 m for C5 and C1, respectively, which also supported the lateral flow of wastewater in the unsaturated zone (Fig. 3a).

The infiltration and mixing processes are very similar to previous research conducted in the deep vadose zone when affected by an unlined wastewater pond (Asaf et al. 2004, Gal et al. 2009). Gal et al. (2009) found that the recharge rate decreased after the wastewater discharge ceased due to the decreasing sediment moisture. Additionally, variation of surface conditions resulted in different distributions of isotope enrichment at vertical depths (Gal et al. 2009). Most  $\delta^2\text{H}$  isotopes of C6 and C0 were greater than the average  $\delta^2\text{H}$  (-49.7‰) in wastewater from September 2008 to June 2011. During extensive evaporation from the unsaturated zone, kinetic effects by vapor diffusion were greater than those of evaporation from open surfaces (Balugani et al., 2021). Therefore, stable isotopes throughout the C6 and C0 profiles enriched more than wastewater in TWR and porewater in C3. When comparing C6 and C0, the fractionation effect from soil evaporation beneath cotton crops was more robust than for soils beneath wheat/maize, with the slopes of the evaporation lines being 2.60 and 4.13, respectively (Fig. 6b). This can be attributed to differences in water balances in the different land uses. The cotton field receives 100 mm of irrigation annually (Min et al., 2018), and the wheat/maize cropping system receives 320–360 mm of irrigation annually (Sun et al., 2006; Zhang et al., 2018). The dryer soil conditions resulted in more substantial

evaporation fractionation, while more irrigation at the wheat/maize fields diluted the isotopic fractionation signal.

#### 4.2. Seasonal recharge and recharge flow paths of USGW

The observed  $\delta^2\text{H}$  vs  $\delta^{18}\text{O}$  relationship of porewaters (USPW), the upper shallow groundwaters (USGW) of C0, C3, C5 and C6, and the calculated  $\delta^2\text{H}$  vs  $\delta^{18}\text{O}$  relationship of the sine wave fitting curves of different seasons for these sites were shown in Fig. 9. The hysteresis loop was found in the observed data and the fitting data of USGW based on the spectral analysis and the exponential model (Table 1). Benettin et al. (2018) reported that residual water samples affected by evaporation show a hysteresis loop and the width of the hysteresis loop depends on the amplitude of the seasonal cycle of evaporation and the extent to which it differs from the seasonal cycle of the isotopes in precipitation. This hysteresis loop was testified by using numerical experiments based on established isotope fractionation theory. The input source of isotopes in precipitation showed sine or cosine curves with semi-annual cycle (Yamanaka et al., 2004) and the variation of isotopes in USGW also showed the semi-annual period correspondingly affected by the seasonal precipitation and irrigation recharge. Fig. 9 displayed the distribution of two loops with a mean hysteresis time of three months. The contribution of each seasonal recharge source determines the loop's shape. As for USGW at C3 influenced by TWR wastewater, the loop is narrow with a nearly straight line of precipitation, and evaporated porewater end-members plot beneath the TWR evaporation line. Samples during summer and winter overlapped with porewaters at shallow depths suggesting a significant contribution of isotopically fractionated porewater on USGW at those times, while samples during fall and spring indicate a dominant impact of (non-fractionated) precipitation. Porewater

contribution to USGW recharge occurred during all seasons at C6, but the contribution of precipitation and SGW increased at C0 site, which resulted in larger loops at the C0 site compared to the C6 site. USGW in irrigated farmlands with low amounts of irrigation and intense evaporation at C6 (cotton lands) had a stronger hysteresis with a loop that overlapped with shallow porewater suggesting a major contribution of porewater.

According to the contribution ratios of different sources (Fig. S5), precipitation also contributed significantly (44 to 61 %) to USGW recharge besides the residual water in the porewater. However, according to the estimation of recharge rates of matrix flow (0.65 ~ 1.09 m/year) from the distribution of porewater isotopes, it is impossible for surface water sources to reach the water table in one year. Consequently, the 3-month average response time indicates that there must have been preferential flow to the USGW (Esit et al., 2021; Zhang et al., 2014). The abrupt changes in porewater isotopes in the sand layers (Fig. 5) suggest that preferential or fast flow (such as lateral groundwater recharge) included re-mobilized evaporated water sources. Many studies conducted on soil water or groundwater in the North China Plain have supported preferential flow, particularly for irrigated farmlands (Ma et al., 2017; Song et al., 2009; Zheng et al., 2020). According to the field survey, preferential flow traced by pollutants was also found in the silt layer and silt clay above 20 m depth (Fig. 3b-d). Therefore, it may be possible that preferential flow contributes to seasonal variation in USGW isotopic signals. Unlike C6, C0-C5 are located in the Tanghe River Channel, and the higher permeability of the preferential flow in the unsaturated zone possesses a shorter mean USGW response time of 100–118 d. Eventually, the USGW downstream is affected by the rapid lateral flow of the sand layer. To facilitate understanding, we synthesized the above discussion of USGW recharge and drew a conceptual

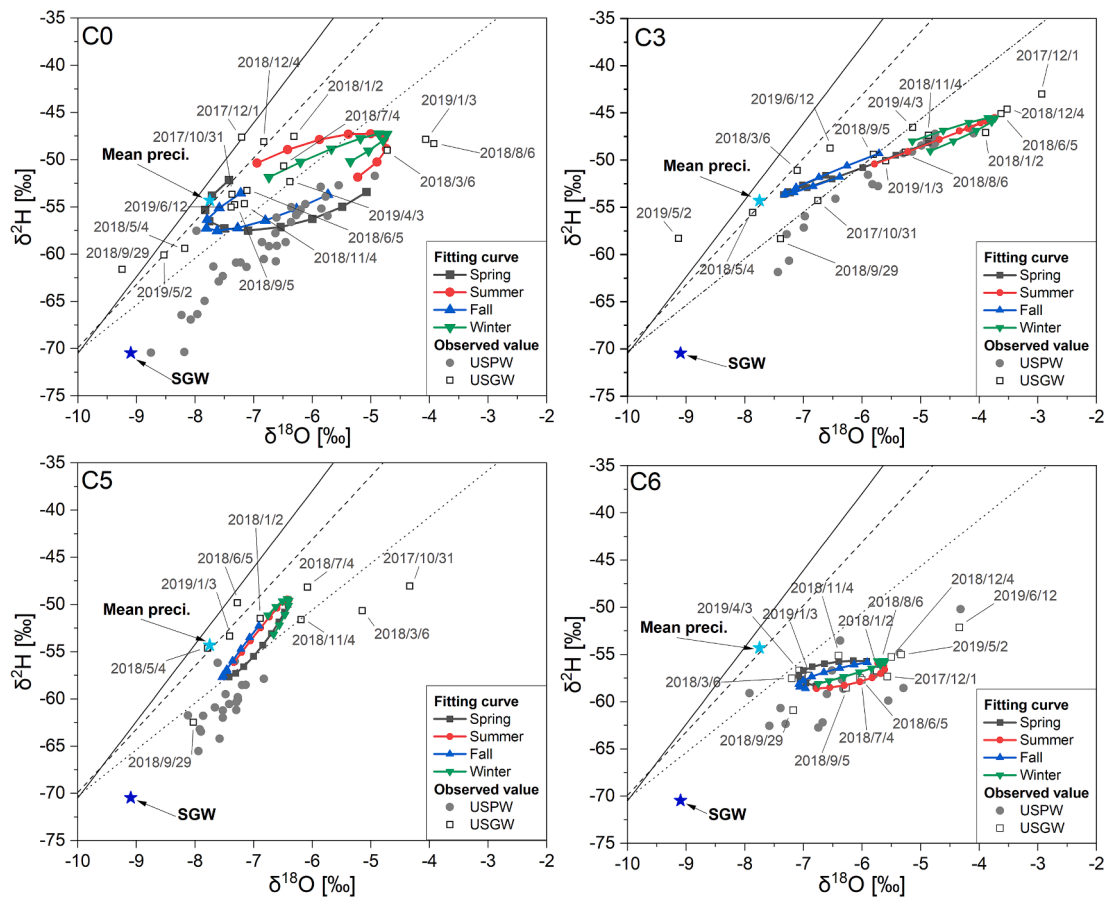


Fig. 9. Relationship between  $\delta^2\text{H}$  and  $\delta^{18}\text{O}$  in the upper shallow groundwater of C0-C6 compared with fitting sine/cosine curves of different seasons. USPW is the porewater in the unsaturated zone, USGW is the upper shallow groundwater, and SGW is the shallow groundwater.

diagram of the TWR upper shallow groundwater recharge model (Fig. 10).

#### 4.3. Impact of preferential flow or lateral flow on USGW quality

Understanding the processes of local groundwater recharge is vital to identify the solute transport in porewater and contamination in groundwater. Besides stable isotopes, major ions in groundwater are good indicators for verifying groundwater processes. Sulphate was the major water ion in wastewater of the TWR, which contributed to variation in water quality (as EC) (Wang et al., 2014). As Fig. 8 shows, the  $\text{SO}_4^{2-}$  was relatively stable due to the infiltration of wastewater with high  $\text{SO}_4^{2-}$  concentrations before June 2018 (Fig. 4). There were large variations after the 2018 rainy season since the  $\text{SO}_4^{2-}$  source was cut off. The dilution effect caused by preferential flow or fast flows of precipitation recharge might be the primary cause of this variation. This is in accordance with the contribution ratio of precipitation (Fig. S5). However, the increased  $\text{SO}_4^{2-}$  concentrations after fast flow recharge indicated the contribution of matrix flow or remobilization of porewater, which had a high  $\text{SO}_4^{2-}$  content (Fig. S6). Similarly, winter and spring irrigation with shallow GW had a similar impact on USGW quality.

The impact of preferential flow and slow matrix flow on  $\text{NO}_3^-$  in USGW is different from  $\text{SO}_4^{2-}$ . A conceptual model of recharge mechanisms of USGW and transportation of pollutants (i.e.,  $\text{NO}_3^-$ ) is presented in Fig. 10. During the infiltration processes of multiple water sources, evaporation, mixing, and recharge rate of matrix flow determine the vertical distribution of isotopes in porewater. Isotopes in aquifers differ from upper layer porewater, but are similar to shallow depth porewater, suggesting the mixing of fast flow. We found that the fast flow significantly contributed to the USGW recharge and increase in  $\text{NO}_3^-$ . Past research has pointed out that  $\text{NO}_3^-$  accumulates in soils to 2 m depth (Chun-Sheng et al., 2011; Ju and Zhang, 2017; Wang et al., 2019), and the amount accumulated decreases with increased depth toward the saturated zone. Generally,  $\text{NO}_3^-$  accumulates during the winter wheat season and leaches into the soil profile during the summer maize season (Lu et al., 2019). In our study, leaching occurred not only in summer but

also in the winter, showing elements of seasonal leaching. This can be attributed to several factors. First, the preferential flow induced by flood irrigation carries the N-fertilizer in surface soil into aquifers. Second, there were many factories around the TWR, and these operations dug seepage pits to store or leak wastewater, as was noted during our field investigations. Farmland was the primary land use type in the study area and also on the plains of the Baiyangdian watershed.  $\text{NO}_3^-$  gets easily transported from the root zone to SGW in farmland. Min et al. (2018) reported for the North China Plain that  $\text{NO}_3^-$  concentrations in peaks above 2 m soil depth ranged from 550 to 812 mg/L for a wheat/maize cropping system and ranged from 260 to 760 mg/L for cotton, and differences between crops were due to different N-application levels. This could also explain why the  $\text{NO}_3^-$  concentrations in the USGW of the wheat/maize crop (C0) were higher than that in the USGW of cotton (C6).

#### 5. Conclusions

We investigated recharge and transport pathways of major pollutants ( $\text{SO}_4^{2-}$  and  $\text{NO}_3^-$ ) from the surface to the upper shallow groundwater (USGW) in an alluvial aquifer as affected by a long-term unlined wastewater reservoir (the TWR). The variation in contributions from many sources created a complex groundwater recharge system. Porewater stable isotopes of sediment profiles recorded the infiltration and mixing processes of different water sources, including precipitation, wastewater leakage, wastewater irrigation, and shallow groundwater irrigation. Matrix flow's average vertical recharge rate ranged from 0.63 to 1.09 m/year. The stable isotopes in sand aquifers were similar to those in porewater at shallow depths in the sediment profiles, suggesting the existence of fast preferential flow pathways.

Shallow groundwater above 30 m showed the seasonal contribution of evaporated water sources, including precipitation, porewater in sediment, and irrigation water from shallow groundwater from 80 to 120 m depths. The preferential flow pathways and lateral flow along the TWR lead to significant precipitation contributions (44 to 61 %) to the USGW recharge for most sites. Hysteresis loops in the dual isotope space

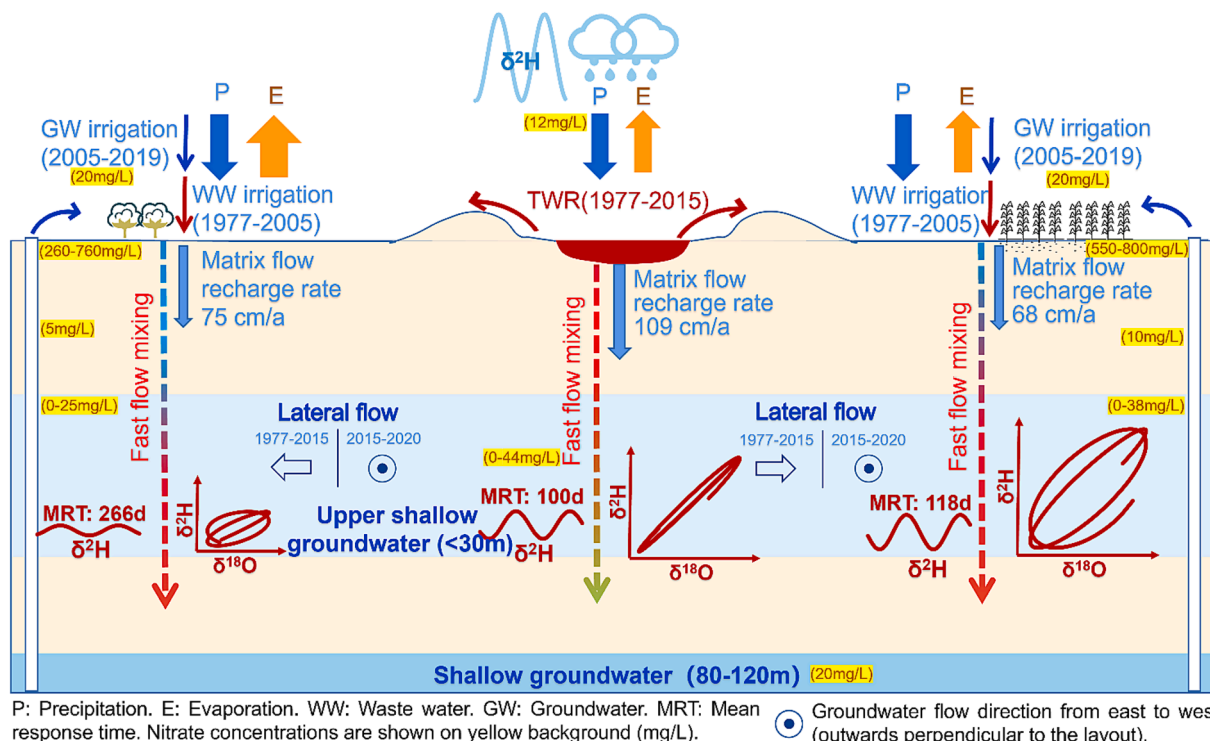


Fig. 10. Conceptual model of the upper shallow groundwater recharge and transport of nitrate affected by multiple sources with seasonal variation.

of seasonal USGW recharge reflected the seasonal variation in different water sources. We found two types of hysteresis loops in the  $\delta^2\text{H}$  and  $\delta^{18}\text{O}$  plot of USGW: 1) USGW in regions influenced by TWR wastewater had narrow loops and a nearly straight line between the end member of precipitation and evaporated porewater TWR leakage; 2) USGW in irrigated farmlands with low and high amounts of irrigation and intense evaporation (i.e., cotton fields and wheat/maize fields) had a stronger hysteresis with loops that overlapped with shallow porewater suggesting all three water sources contributed to the groundwater recharge. The deviation from the LMWL showed differences in the magnitude of evaporation. Therefore, we hypothesize that the shape of the hysteresis loop in the  $\delta^2\text{H}$  vs  $\delta^{18}\text{O}$  plot for USGW was determined by the varying dominance of different recharge sources. This novel interpretation is transferrable and could identify other groundwater aquifers under threat of contamination.

The seasonal recharge also contributed to the seasonal variation of the USGW quality. The  $\text{SO}_4^{2-}$  concentrations slightly decreased due to dilution. However, the  $\text{NO}_3^-$  concentrations increased after precipitation and irrigation when preferential flow carried nutrients from the shallow soil depths into the aquifer. Therefore, long-term wastewater leakage and irrigation affected local recharge and sediment pollutants, and these measures should receive greater attention. Action is needed to prevent pollutant transport by preferential and fast flow in alluvial aquifers, as these systems are highly susceptible to contamination.

#### CRedit authorship contribution statement

**Shiqin Wang:** Writing – original draft, Methodology, Supervision. **Zhixiong Zhang:** Visualization, Formal analysis, Investigation, Writing – review & editing. **Matthias Sprenger:** Writing – review & editing. **Shoucai Wei:** . **Wenbo Zheng:** . **Binbin Liu:** . **Yanjun Shen:** . **Yizhang Zhang:** .

#### Declaration of Competing Interest

The authors declare that they have no known competing financial interests or personal relationships that could have appeared to influence the work reported in this paper.

#### Data availability

No data was used for the research described in the article.

#### Acknowledgments

The study was supported by the National Natural Science Foundation of China (No.42071053; 442377080), the National Key R&D Program of China (2021YFD1700500), and the Foundation for Innovative Research Groups of the Natural Science Foundation of Hebei Province (D2021503001).

#### Appendix A. Supplementary data

Supplementary data to this article can be found online at <https://doi.org/10.1016/j.jhydrol.2023.130424>.

#### References

- Balugani, E., Lubczynski, M.W., Metselaar, K., 2021. Evaporation Through a Dry Soil Layer: Column Experiments. *Water Resour. Res.* 57 (8), e2020WR028286 <https://doi.org/10.1029/2020WR028286>.
- Beckers, L.-M., Brack, W., Dann, J.P., Krauss, M., Müller, E., Schulze, T., 2020. Unraveling longitudinal pollution patterns of organic micropollutants in a river by non-target screening and cluster analysis. *Sci. Total Environ.* 727, 138388.
- Beddows, P.A., Mandić, M., Ford, D.C., Schwarcz, H.P., 2016. Oxygen and hydrogen isotopic variations between adjacent drips in three caves at increasing elevation in a temperate coastal rainforest, Vancouver Island, Canada. *Geochim. Cosmochim. Acta* 172, 370–386. <https://doi.org/10.1016/j.gca.2015.08.017>.

- Benettin, P., Volkman, T.H.M., von Freyberg, J., Frentress, J., Penna, D., Dawson, T.E., Kirchner, J.W., 2018. Effects of climatic seasonality on the isotopic composition of evaporating soil waters. *Hydrol. Earth Syst. Sci.* 22 (5), 2881–2890.
- Chen, H., Hu, K., Nie, Y., Wang, K., 2017. Analysis of soil water movement inside a footslope and a depression in a karst catchment. *Southwest China. Scientific Reports* 7 (1), 2544. <https://doi.org/10.1038/s41598-017-02619-x>.
- Chun-Sheng, H.U., et al., 2011. Nitrogen flux and its manipulation in the cropland ecosystem of the North China Plain. *Chin. J. Eco-Agric.* 19 (5), 997–1003.
- Craig, H., 1961. Isotopic variations in meteoric waters. *Science* 133 (3465), 1702–1703.
- Dansgaard, W., 1964. Stable isotopes in precipitation. *Tellus* 16 (4), 436–468. <https://doi.org/10.1111/j.2153-3490.1964.tb00181.x>.
- Das, P., Mukherjee, A., Lapworth, D.J., Das, K., Bhaumik, S., Layek, M.K., Shaw, A., Smith, M., Sengupta, P., MacDonald, A.M., Sen, J., 2021. Quantifying the dynamics of sub-daily to seasonal hydrological interactions of Ganges river with groundwater in a densely populated city: Implications to vulnerability of drinking water sources. *J. Environ. Manage.* 288, 112384 <https://doi.org/10.1016/j.jenvman.2021.112384>.
- de Vries, J.J., Simmers, I., 2002. Groundwater recharge: an overview of processes and challenges. *Hydrgeol. J.* 10 (1), 5–17. <https://doi.org/10.1007/s10040-001-0171-7>.
- Esit, M., Kumar, S., Pandey, A., Lawrence, D.M., Rangwala, I., Yeager, S., 2021. Seasonal to multi-year soil moisture drought forecasting. *Npj Climate and Atmospheric Science* 4 (1). <https://doi.org/10.1038/s41612-021-00172-z>.
- Filippini, M., Stumpp, C., Nijenhuis, I., Richnow, H.H., Gargini, A., 2015. Evaluation of aquifer recharge and vulnerability in an alluvial lowland using environmental tracers. *J. Hydrol.* 529, 1657–1668. <https://doi.org/10.1016/j.jhydrol.2015.07.055>.
- Gal, H., Weisbrod, N., Dahan, O., Ronen, Z., Nativ, R., 2009. Perchlorate accumulation and migration in the deep vadose zone in a semiarid region. *J. Hydrol.* 378 (1–2), 142–149. <https://doi.org/10.1016/j.jhydrol.2009.09.018>.
- Garvelmann, J., Kulls, C., Weiler, M., 2012. A porewater-based stable isotope approach for the investigation of subsurface hydrological processes. *Hydrol. Earth Syst. Sci.* 16 (2), 631–640. <https://doi.org/10.5194/hess-16-631-2012>.
- Gelhar, L.W., Wilson, J.L., 1974. Ground-Water Quality Modelinga. *Ground-Water Quality Modelinga. Groundwater* 12 (6), 399–408.
- Grande, E., Visser, A., Moran, J.E., 2020. Catchment storage and residence time in a periodically irrigated watershed. *Hydrol. Process.* 34 (14), 3028–3044. <https://doi.org/10.1002/hyp.13798>.
- He, B., Guan, Q., 2020. A mathematical approach to improving the representation of surface water-groundwater exchange in the hyporheic zone. *J. Water Clim. Change* 12 (5), 1788–1801. <https://doi.org/10.2166/wcc.2020.162>.
- Houben, T., Pujades, E., Kalbacher, T., Dietrich, P., Attinger, S., 2022. From Dynamic Groundwater Level Measurements to Regional Aquifer Parameters—Assessing the Power of Spectral Analysis. *Water Resour. Res.* 58 (5), e2021WR031289 <https://doi.org/10.1029/2021WR031289>.
- Ishii, E., Watanabe, Y., Agusa, T., Hosono, T., Nakata, H., 2021. Acesulfame as a suitable sewer tracer on groundwater pollution: A case study before and after the 2016 Mw 7.0 Kumamoto earthquakes. *Sci. Total Environ.* 754, 142409 <https://doi.org/10.1016/j.scitotenv.2020.142409>.
- Jasechko, S., 2019. Global isotope hydrogeology—Review. *Rev. Geophys.* 57 (3), 835–965.
- Ju, X.-T., Zhang, C., 2017. Nitrogen cycling and environmental impacts in upland agricultural soils in North China: A review. *J. Integr. Agric.* 16 (12), 2848–2862. [https://doi.org/10.1016/S2095-3119\(17\)61743-X](https://doi.org/10.1016/S2095-3119(17)61743-X).
- Lee, K.S., Kim, J.M., Lee, D.R., Kim, Y., Lee, D., 2007. Analysis of water movement through an unsaturated soil zone in Jeju Island, Korea using stable oxygen and hydrogen isotopes. *J. Hydrol.* 345 (3–4), 199–211. <https://doi.org/10.1016/j.jhydrol.2007.08.006>.
- Lu, J., Bai, Z., Velthof, G.L., Wu, Z., Chadwick, D., Ma, L., 2019. Accumulation and leaching of nitrate in soils in wheat-maize production in China. *Agric Water Manag* 212, 407–415.
- Ma, B., Liang, X., Liu, S., Jin, M., Nimmo, J.R., Li, J., 2017. Evaluation of diffuse and preferential flow pathways of infiltrated precipitation and irrigation using oxygen and hydrogen isotopes. *Hydrgeol. J.* 25 (3), 675–688.
- Ma, B., Jin, M., Liang, X., Li, J., 2019. Application of environmental tracers for investigation of groundwater mean residence time and aquifer recharge in fault-influenced hydraulic drop alluvium aquifers. *Hydrol. Earth Syst. Sci.* 23 (1), 427–446.
- McCance, W., Jones, O.A.H., Cendón, D.I., Edwards, M., Surapaneni, A., Chadalavada, S., Wang, S., Currell, M., 2020. Combining environmental isotopes with Contaminants of Emerging Concern (CECs) to characterise wastewater derived impacts on groundwater quality. *Water Res.* 182, 116036 <https://doi.org/10.1016/j.watres.2020.116036>.
- McGuire, K., DeWalle, D., Gburek, W., 2002. Evaluation of mean residence time in subsurface waters using oxygen-18 fluctuations during drought conditions in the mid-Appalachians. *J. Hydrol.* 261 (1–4), 132–149.
- Min, L.L., Shen, Y.J., Pei, H.W., Wang, P., 2018. Water movement and solute transport in deep vadose zone under four irrigated agricultural land-use types in the North China Plain. *J. Hydrol.* 559, 510–522. <https://doi.org/10.1016/j.jhydrol.2018.02.037>.
- Niraula, R., Meixner, T., Ajami, H., Rodell, M., Gochis, D., Castro, C.L., 2017. Comparing potential recharge estimates from three Land Surface Models across the western US. *J. Hydrol.* 545, 410–423.
- Raihan, A.T., Bauer, S., Mukhopadhyaya, S., 2022. An AHP based approach to forecast groundwater level at potential recharge zones of Uckermark District, Brandenburg. *Germany. Sci Rep* 12 (1), 6365. <https://doi.org/10.1038/s41598-022-10403-9>.
- Rodgers, P., Soulsby, C., Waldron, S., Tetzlaff, D., 2005. Using stable isotope tracers to assess hydrological flow paths, residence times and landscape influences in a nested mesoscale catchment. *Hydrol. Earth Syst. Sci.* 9 (3), 139–155. <https://doi.org/10.5194/hess-9-139-2005>.

- K. Rozanski L. Araguás-Araguás R. Gonfiantini Isotopic Patterns in Modern Global Precipitation, Climate Change in Continental Isotopic Records 1993 10.1029/GM078p0001 1 36.
- Sánchez-Murillo, R., Birkel, C., 2016. Groundwater recharge mechanisms inferred from isoscapes in a complex tropical mountainous region. *Geophys. Res. Lett.* 43 (10), 5060–5069. <https://doi.org/10.1002/2016GL068888>.
- Song, X., Wang, S., Xiao, G., Wang, Z., Liu, X., Wang, P., 2009. A study of soil water movement combining soil water potential with stable isotopes at two sites of shallow groundwater areas in the North China Plain. *Hydrol. Process.* 23 (9), 1376–1388.
- Sprenger, M., Leistert, H., Gimbel, K., Weiler, M., 2016. Illuminating hydrological processes at the soil-vegetation-atmosphere interface with water stable isotopes. *Rev. Geophys.* 54 (3), 674–704. <https://doi.org/10.1002/2015rg000515>.
- Stahl, M.O., Gehring, J., Jameel, Y., 2020. Isotopic variation in groundwater across the conterminous United States – Insight into hydrologic processes. *Hydrol. Process.* 34 (16), 3506–3523. <https://doi.org/10.1002/hyp.13832>.
- Sun, X., Lin, J., Gu, W., Min, X., Han, J., Dai, Y., Liu, P., Wang, S., 2021. Analysis and evaluation of the renewability of the deep groundwater in the Huaihe River Basin, China. *Environmental Earth Sciences* 80 (3). <https://doi.org/10.1007/s12665-020-09355-y>.
- Sun, H.-Y., Liu, C.-M., Zhang, X.-Y., Shen, Y.-J., Zhang, Y.-Q., 2006. Effects of irrigation on water balance, yield and WUE of winter wheat in the North China Plain. *Agric Water Manag* 85 (1–2), 211–218.
- Tekleab, S., Wenninger, J., Uhlenbrook, S., 2014. Characterisation of stable isotopes to identify residence times and runoff components in two meso-scale catchments in the Abay/Upper Blue Nile basin, Ethiopia. *Hydrology and Earth System Sciences* 18 (6), 2415–2431. <https://doi.org/10.5194/hess-18-2415-2014>.
- Tipple, B.J., Jameel, Y., Chau, T.H., Mancuso, C.J., Bowen, G.J., Dufour, A., Chesson, L. A., Ehleringer, J.R., 2017. Stable hydrogen and oxygen isotopes of tap water reveal structure of the San Francisco Bay Area's water system and adjustments during a major drought. *Water Res.* 119, 212–224.
- Tweed, S., Massuel, S., Seidel, J.L., Chhuon, K., Lun, S., Eang, K.E., Venot, J.P., Belaud, G., Babic, M., Leblanc, M., 2020. Seasonal in fluences on groundwater arsenic concentrations in the irrigated region of the Cambodian Mekong Delta. *Sci. Total Environ.* 728, 138598.
- Vystavna, Y., Schmidt, S.I., Diadin, D., Rossi, P.M., Vergeles, Y., Erostate, M., Yermakovich, I., Yakovlev, V., Knöller, K., Vadillo, I., 2019. Multi-tracing of recharge seasonality and contamination in groundwater: A tool for urban water resource management. *Water Res.* 161, 413–422.
- Wang, S., Shao, J., Song, X., Zhang, Y., Huo, Z., Zhou, X., 2008. Application of MODFLOW and geographic information system to groundwater flow simulation in North China Plain, China. *Environ. Geol.* 55 (7), 1449–1462.
- Wang, S., Tang, C., Song, X., Yuan, R., Wang, Q., Zhang, Y., 2013. Using major ions and  $\delta^{15}\text{N}$ - $\text{NO}_3^-$  to identify nitrate sources and fate in an alluvial aquifer of the Baiyangdian lake watershed, North China Plain. *Environ. Sci. Processes Impacts* 15 (7), 1430.
- Wang, S., Tang, C., Song, X., Wang, Q., Zhang, Y., Yuan, R., 2014. The impacts of a linear wastewater reservoir on groundwater recharge and geochemical evolution in a semi-arid area of the Lake Baiyangdian watershed, North China Plain. *Sci. Total Environ.* 482–483, 325–335.
- Wang, S., Wei, S., Liang, H., Zheng, W., Li, X., Hu, C., Currell, M.J., Zhou, F., Min, L., 2019. Nitrogen stock and leaching rates in a thick vadose zone below areas of long-term nitrogen fertilizer application in the North China Plain: A future groundwater quality threat. *J. Hydrol.* 576, 28–40.
- Wright, S.N., Novakowski, K.S., 2019. Groundwater recharge, flow and stable isotope attenuation in sedimentary and crystalline fractured rocks: Spatiotemporal monitoring from multi-level wells. *J. Hydrol.* 571, 178–192. <https://doi.org/10.1016/j.jhydrol.2019.01.028>.
- Wu, M., Wu, J., Liu, J., Wu, J., Zheng, C., 2015. Effect of groundwater quality on sustainability of groundwater resource: A case study in the North China Plain. *J. Contam Hydrol* 179, 132–147. <https://doi.org/10.1016/j.jconhyd.2015.06.001>.
- Yamanaka, T., Shimada, J., Hamada, Y., Tanaka, T., Yang, Y., Zhang, W., Hu, C., 2004. Hydrogen and oxygen isotopes in precipitation in the northern part of the North China Plain: climatology and inter-storm variability. *Hydrol Process* 18:2211–2222 (Special issue: water crises and hydrology in North China). *Hydrological Processes*, 18: 2211–2222. doi:10.1002/hyp.5525.
- Yang, Y., Shang, X.u., Chen, Z., Mei, K., Wang, Z., Dahlgren, R.A., Zhang, M., Ji, X., 2021. A support vector regression model to predict nitrate-nitrogen isotopic composition using hydro-chemical variables. *J Environ Manage* 290, 112674. <https://doi.org/10.1016/j.jenvman.2021.112674>.
- Yuan, R.Q., Wang, S.Q., Wang, P., Song, X.F., Tang, C.Y., 2017. Changes in flow and chemistry of groundwater heavily affected by human impacts in the Baiyangdian catchment of the North China Plain. *Environ. Earth Sci.* 76 (16), 19. <https://doi.org/10.1007/s12665-017-6918-9>.
- Yuan, R., Wang, M., Wang, S., Song, X., 2020. Water transfer imposes hydrochemical impacts on groundwater by altering the interaction of groundwater and surface water. *J. Hydrol.* 583, 124617. <https://doi.org/10.1016/j.jhydrol.2020.124617>.
- Zhang, Y., Lei, H., Zhao, W., Shen, Y., Xiao, D., 2018. Comparison of the water budget for the typical cropland and pear orchard ecosystems in the North China Plain. *Agric Water Manag* 198, 53–64.
- Zhang, J., Lin, H., Doolittle, J., 2014. Soil layering and preferential flow impacts on seasonal changes of GPR signals in two contrasting soils. *Geoderma* 213, 560–569. <https://doi.org/10.1016/j.geoderma.2013.08.035>.
- Zheng, W., Wang, S., Tan, K., Lei, Y., 2020. Nitrate accumulation and leaching potential is controlled by land-use and extreme precipitation in a headwater catchment in the North China Plain. *Sci. Total Environ.* 707, 136168.
- Zhou, J., Liu, G., Meng, Y., Xia, ChengCheng, Chen, K.e., Chen, Y.u., 2021. Using stable isotopes as tracer to investigate hydrological condition and estimate water residence time in a plain region, Chengdu, China. *Scientific Reports* 11 (1). <https://doi.org/10.1038/s41598-021-82349-3>.